catalysts

MDPI

Article

Au@CoS-$BiVO_4$ {010} Constructed for Visible-Light-Assisted Peroxymonosulfate Activation

Yekun Ji [1,†], Ye Zhou [1,†], Jinnan Wang [1,*], Aimin Li [1], Weilin Bian [2] and Philippe François-Xavier Corvini [3]

[1] State Key Laboratory of Pollution Control and Resource Reuse & School of the Environment Nanjing University, Nanjing 210023, China; yekun_ji@163.com (Y.J.); 17379310917@163.com (Y.Z.); liaimin99@nju.edu.cn (A.L.)
[2] Institute of Water Environmental Engineering & Technology, Yancheng 224000, China; bianweilin1987@163.com
[3] School of Life Sciences, University of Applied Sciences and Arts Northwestern Switzerland, 4132 Basel, Switzerland; philippe.corvini@fhnw.ch
* Correspondence: wjnnju@163.com
† First author: Y. K. Ji and Y. Zhou.

Abstract: A visible-light-Fenton-like reaction system was constructed for the selective conversion of peroxymonosulfate to sulfate radical. Au@CoS, when doped on monoclinic $BiVO_4$ {010} facets, promoted spatial charge separation due to the different energy band between the m-$BiVO_4$ {010} and {110} facets. The visible-light response of m-$BiVO_4$ was enhanced, which was attributed to the SPR effect of Au. And the photogenerated electrons were transferred from the m-$BiVO_4$ {010} facet to Au via a Schottky junction. Owing to higher work function, CoS was able to capture these photoelectrons with acceleration of the Co(II)/Co(III) redox, enhancing peroxymonosulfate conversion to sulfate radical ($Co^{2+} + HSO_5^- \rightarrow Co^{3+} + \bullet SO_4^- + OH^-$). On the other hand, holes accumulated on m-$BiVO_4$ {110} facets also contributed to organics oxidation. Thus, more than 95% of RhB was degraded within 40 min, and, even after five cycles, over 80% of RhB could be removed. The radical trapping experiments and EPR confirmed that both the sulfate radical and photogenerated hole were the main species for organics degradation. UV-vis DRS, photoluminescence (PL) and photoelectrochemical analyses also confirmed the enhancement of the visible-light response and charge separation. In a pilot scale experiment (PMS = 3 mM, initial TOC = 151 mg/L, reaction time = 4 h), CoS-Au-$BiVO_4$ loaded on glass fiber showed a high mineralization rate (>60%) of practical wastewater.

Keywords: visible-light-assisted peroxymonosulfate activation; CoS-Au-$BiVO_4$ {010}; spatial charge separation; electron sink; heterostructure

check for updates

Citation: Ji, Y.; Zhou, Y.; Wang, J.; Li, A.; Bian, W.; Corvini, P.F.-X. Au@CoS-$BiVO_4$ {010} Constructed for Visible-Light-Assisted Peroxymonosulfate Activation. *Catalysts* **2021**, *11*, 1414. https://doi.org/10.3390/catal11111414

Academic Editor: Salvatore Scirè

Received: 25 September 2021
Accepted: 13 November 2021
Published: 22 November 2021

1. Introduction

Owing to its higher oxidative potential (E^0 = 2.5–3.1 V) and longer half-life ($t_{1/2}$ = 30–40 μs), sulfate radical ($SO_4^-\bullet$) could degrade organics more efficiently than OH• (E^0 = 2.80 V, $t_{1/2}$ = <1 μs) in neutral solutions [1,2]. Various transition metals (Fe, Cu, Mn and Co, etc.) were applied as activators for the enhancement of peroxymonosulfate (PMS) conversion to $\bullet SO_4^-$ [3–6]. Cobalt oxides were considered as a promising catalyst for PMS activation, due to their high standard reduction potential (E^0 = +1.92 V vs. NHE) [7–9]. However, during the Fenton-like reaction process, PMS reacts not only with Co(II) as the electron acceptor ($Co^{2+} + HSO_5^- \rightarrow Co^{3+} + \bullet SO_4^- + OH^-$) but also with Co(III) as the electron donor ($Co^{3+} + HSO_5^- \rightarrow Co^{2+} + \bullet SO_5^- + OH^-$), accompanied by the accumulation of Co(III) and the invalid decomposition of peroxymonosulfate [3].

To retard accumulation of high-valence-state transition metal (HVTM), photo-Fenton-like reaction systems were designed in which HVTM might be reduced by photoelectrons [10–13]. Additionally, the pre-spatial separation effect of semiconductors (TiO_2 and $BiVO_4$ et al.) [14–16] was attempted to improve the photogenerated electrons migration for HVTM reduction. Due to the different energy levels of the CB and VB between {010}

and {110} facets, $BiVO_4$ could act as the 'pre-separation channel' to achieve spatial charge separation [15]. In addition, the efficient utilization of these photogenerated carriers also played an important role in activity, as these photogenerated carriers were transferred from catalyst bulk to surface [17–20]. Previous research demonstrated that more than 60% of the photogenerated carriers of m-$BiVO_4$ were recombined before they were transferred from bulk phase to the surface because photogenerated electrons (CB = 0.3 eV) cannot reduce the dissolved O_2 in water to produce O_2^-(E_0 ($O_2/\cdot O_2^-$ = −0.33 V vs. NHE) [21,22].

On the other hand, as widely used co-catalysts, noble metals (Au, Pt, Pd) with low Fermi level could construct Schottky junctions with semiconductors, which could act as photogenerated electron sinks for preventing the recombination of photogenerated carriers [23–25]. To transport and utilize photoelectrons, various heterojunctions were constructed [26–28]. HIROAKI TADA constructed a Z-scheme of CdS–Au–TiO_2, in which nanojunctions induced the photoexcited electrons to transfer from TiO2 to Au and, subsequently, from Au to CdS [29]. Notably, in the photo-Fenton-reaction system, these photogenerated electrons, which were transferred by the semiconductor, could not only to accelerate the redox of the transition metal, but also to improve oxidant activation [30–33]. Wang demonstrated that the modification of WO_3 on $FeWO_4/Fe_2O_3$ could promote the transference of photoelectrons from the CB (WO_3) to $FeWO_4/Fe_2O_3$, which promoted the reduction of Fe^{3+} to Fe^{2+} and H_2O_2 selection to ·OH [11]. Thus, it is reasonable that the deposition of transition metal on noble metals can capture photogenerated electrons for the improvement of the transition metal redox and oxidant activation in a photo-Fenton-like reaction system.

Herein, the visible-light response photocatalyst CoS-Au-{010}$BiVO_4$ was designed for PMS activation. Due to the pre-spatial separation effect, photogenerated electrons are transferred to {010} facets. The co-catalyst Au (5.1 eV) with a low Fermi level can construct Schottky junction with $BiVO_4$ {010} facets for accelerating the transference of the photoelectrons from $BiVO_4$ to Au [34,35]. Additionally, the surface plasmon resonance (SPR) of Au particles extends the response range of visible light [36–38]. With the more positive CB (E_{CB} = 0.7 eV) and higher work function of CoS (5.17 eV), photogenerated electrons of Au-{010}$BiVO_4$ were accumulated on CoS [20,39]. Although the photogenerated electrons of $BiVO_4$ (E_{CB} = 0.3 eV) cannot reduce O_2 to $\bullet O_2^-$ (E_0 ($O_2/\bullet O_2^-$ = −0.33 V vs. NHE), these photogenerated electrons can reduce Co(III) (E (Co^{3+}/Co^{2+}) = 1.82 V vs. NHE) to Co(II), which accelerated the redox of Co(II)/Co(III) and the PMS conversion to $\bullet SO_4^-$. Meanwhile, photogenerated holes, which are attributed to the efficient separation and utilization of the photogenerated electrons, can be accumulated on $BiVO_4$ {110} facets and also play an important role in organics degradation. In order to evaluate the potential of CoS-Au-{010}$BiVO_4$, the present work focused on the following aspects: (1) to construct the PMS/Vis/CoS-Au-{010}$BiVO_4$ system and characterize the photo-Fenton catalyst; (2) to evaluate the catalysis activity and stability of PMS/Vis/CoS-Au-{010}$BiVO_4$ system by RhB degradation tests; and (3) to propose possible catalytic mechanisms.

2. Results and Discussion

2.1. Catalysts Characterization

The SEM morphologies (Figure 1A) of the as-synthesized $BiVO_4$ show a smooth surface and monoclinic scheelite crystal structure with exposure of {010} and {110} facets. The heterojunction between the exposed facets was able to facilitate the accumulation of photogenerated electrons on the m-$BiVO_4$ {010} facets on which Au^{3+} ($HAuCl_4 \cdot 3H_2O$) was able to be reduced to Au by capturing photogenerated electrons. Therefore, Au NPs (average size around 80 nm) were selectively photo-deposited on the m-$BiVO_4$ {010} facets which was observed by SEM and energy dispersive spectrum (EDS) of Au-$BiVO_4$ (Figure 1B). The nano-size and uniform distribution of the Au NPs were beneficial for photocatalytic performance. After the photo-deposition of the Au NPs, S was able to be adsorbed on Au NPs and then reduced to S^{2-} by the photogenerated electrons, resulting in the production of CoS with the addition of Co^{2+}. Thus, after photo-deposition of CoS,

the size of the NPs increased, and the surface became rough (Figure 1C). EDS (Figure 1D) also demonstrated that the sample consisted of Bi, V, O, Au, Co and S elements. In addition, TEM showed that the Au NPs were tightly anchored on the surface of the $BiVO_4$ nanocrystals, and CoS with a rough surface was deposited on the Au NPs (Figure 1F). EDX elements mapping of CoS-Au-$BiVO_4$ (Figure 1H) further confirmed the formation of core-shell Au@CoS on $BiVO_4$. However, the HRTEM image (Figure 1G) shows poor crystallinity of CoS, which was proven by XRD analysis (Figure 2).

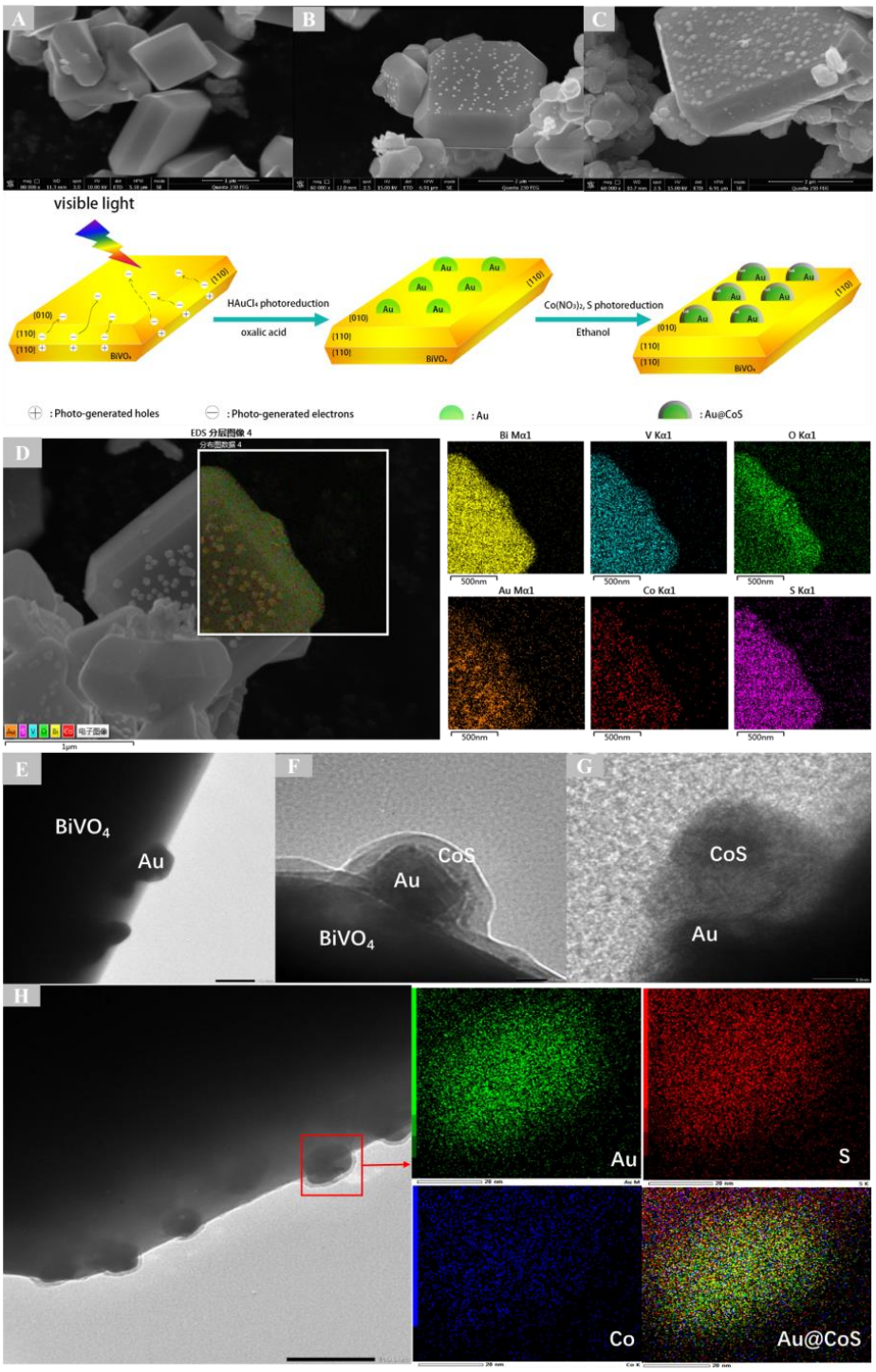

Figure 1. SEM morphologies of $BiVO_4$ (**A**), Au-$BiVO_4$ (**B**) and CoS-Au-$BiVO_4$ (**C**). EDS images for different elements in CoS-Au-$BiVO_4$ (**D**). TEM images of Au-$BiVO_4$ (**E**) and CoS-Au-$BiVO_4$ (**F**,**G**). EDX images for Au, S and Co in CoS-Au-$BiVO_4$ (**H**).

In the spectra of X-ray diffraction (XRD) (Figure 2), it could be observed that the characteristic diffraction peaks of m-$BiVO_4$ were consistent with the monoclinic scheelite crystal structure (JCPDS 14-0688). Peaks at 2θ values of 38.2° and 44.3° appear after the photo-deposition of Au, which are ascribed, respectively, to the (111) and (200) crystal facets of Au (JCPDS 80-0019). Although the characteristic peak of CoS is not observed in the XRD spectra of CoS-Au-$BiVO_4$, EDS still confirms the existence of CoS in the photocatalyst. This phenomenon was also reported in some previous literature, which might be explained by the low content and amorphous structure of CoS in the catalyst composite [40].

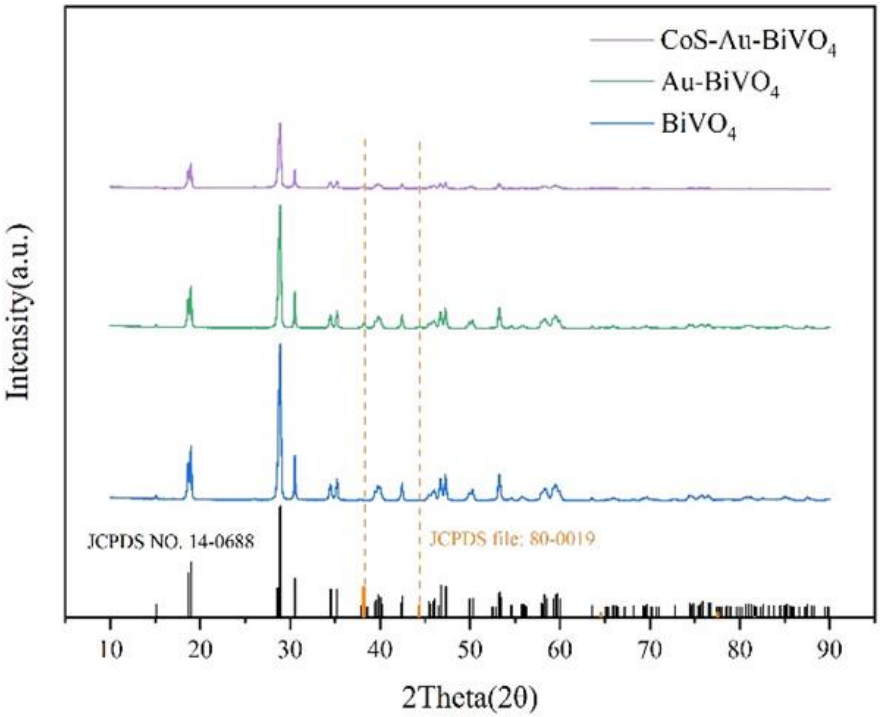

Figure 2. XRD images of $BiVO_4$, Au-$BiVO_4$ and CoS-Au-$BiVO_4$.

X-ray photoelectron spectroscopy (XPS) of CoS-Au-$BiVO_4$ (Figure 3A) demonstrated the existence of elements and their valence on the catalyst surface. Peaks at 84.05 eV and 87.73 eV were ascribed to the Au $4f_{7/2}$ and Au $4f_{5/2}$ of metallic Au, respectively. Since the characteristic peak of S 2p at 164 eV is very close to the characteristic peak of Bi $4f_{5/2}$ (162 eV), the strong peak of Bi $4f_{5/2}$ might shelter the peak of S2p. Thus, the characteristic peak of S2s at 228 eV was selected to calculate the element content of S. The atomic ratios in the CoS-Au-$BiVO_4$ composite could be calculated according to the characteristic peak area of Bi4f, V2p3, O1s, Au4f, Co2p3 and S2s (Table S1). This indicated that the ratio of Co/S was about 1, confirming the existence of CoS in the catalyst. The high-resolution Co 2p spectrum was observed, with binding energy of 779.89 eV, 780.79 eV, 784.97eV, which were assigned, respectively, to Co^{3+} $2p_{3/2}$, Co^{2+} $2p_{3/2}$ and shakeup satellites (Figure 3B,C). In addition, the characteristic peak of Co^{2+} $2p_{3/2}$ (780.79 eV) was much stronger than that of Co^{3+} $2p_{3/2}$ (779.89 eV), suggesting that most of Co elements in the composites were Co^{2+}. As PMS was added to the mixture (CoS-Au-$BiVO_4$/PMS/RhB) without irradiation, the ratio of Co^{2+}/Co^{3+} significantly decreased. It indicated that large amounts of Co^{2+} were oxidized to Co^{3+} by PMS. However, the ratio of Co^{2+}/Co^{3+} was obviously increased to 7.25 after irradiation (Figure 3D), which might be attributed to the reduction of Co^{3+} by photoelectrons.

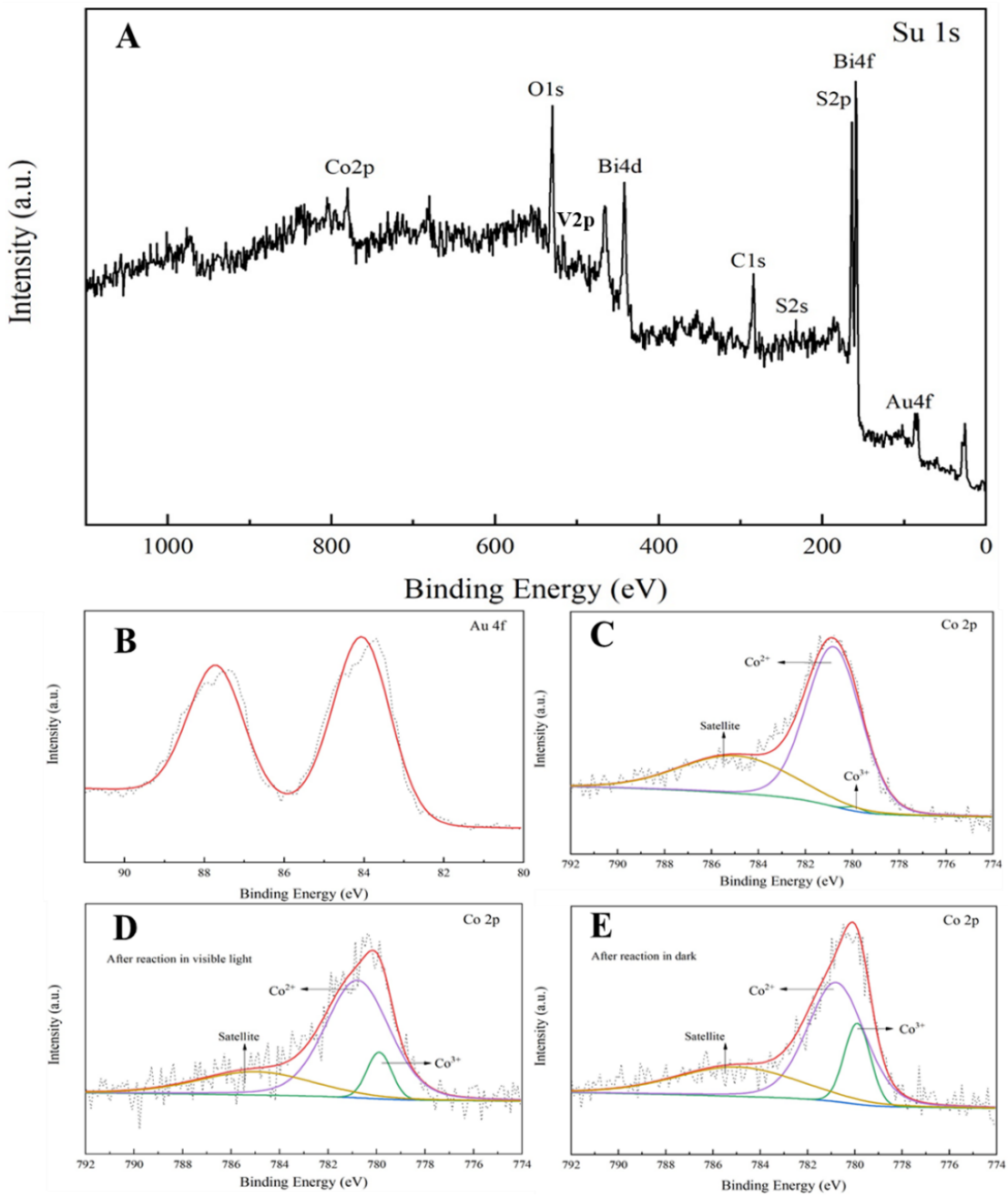

Figure 3. XPS spectra of CoS-Au-$BiVO_4$. (**A**) Survey, (**B**) Au 4f, (**C**) Co 2p, (**D**) Co 2p after reaction in visible light, (**E**) Co 2p after reaction in the dark.

The UV-vis DRS was measured to characterize the light absorption and bandgap (Eg) of samples. The absorption edge of pure $BiVO_4$ at around 550 nm exhibits visible-light response. After the photo-deposition of Au NPs on the $BiVO_4$ {010} facets, the wavelength of visible light response extends from 550 nm to 650 nm because of the surface plasmon resonance (SPR) effect. Although the light harvesting curve of CoS-Au-$BiVO_4$ is similar to that of Au-$BiVO_4$, the characteristic absorption peak of Au shifts from 666.5 to 704.5. This red shift was due to that the transfer of photoelectrons from Au NPs to CoS could decrease the density of electrons in Au [29,41]. The bandgap energies (Eg) are calculated by the Tauc's equation: $(\alpha h\upsilon)^2 = A(h\upsilon - Eg)^n$. Herein, n value is 1 for the direct electronic transition semiconductor of $BiVO_4$. The Tauc plot indicates that the Eg of CoS-Au-$BiVO_4$ (2.36 eV) is narrower than those of Au-$BiVO_4$ (2.38 eV) and $BiVO_4$ (2.41 eV). Thus, CoS-Au-$BiVO_4$ exhibits the strongest visible-light response. Notably, although the characteristic

peak of CoS was not observed in the XRD spectra, the enhanced visible light absorption (550–1000 nm) after the deposition of CoS on $BiVO_4$ still confirmed the existence of CoS in the catalyst. As previous literature reported, the narrow bandgap of CoS broadens the region of light response [42].

The PL intensity of photocatalysts in Figure 4C can be useful to analyze the efficiency of the photogenerated carriers' separation in semiconductors. As expected, CoS-Au-$BiVO_4$ shows the lowest PL intensity, indicating the efficient inhibition of the recombination. Meanwhile, the fluorescence lifetime was prolonged from 2.25 ns to 3.39 ns as Au and CoS were loaded on $BiVO_4$ (Figure 4D). In addition, the photocurrent intensity of CoS-Au-$BiVO_4$ (1.2 $\mu A \cdot cm^{-2}$) was much stronger than that of Au-$BiVO_4$ (0.4 $\mu A \cdot cm^{-2}$) and $BiVO_4$ (0.2 $\mu A \cdot cm^{-2}$), also suggesting the highest photovoltaic conversion. In EIS measurements, the spectra of CoS-Au-$BiVO_4$ show the smallest semicircle, indicating the lowest charge transfer resistance, which demonstrates that CoS-Au-$BiVO_4$ exhibits the highest separation efficiency of the photogenerated carriers.

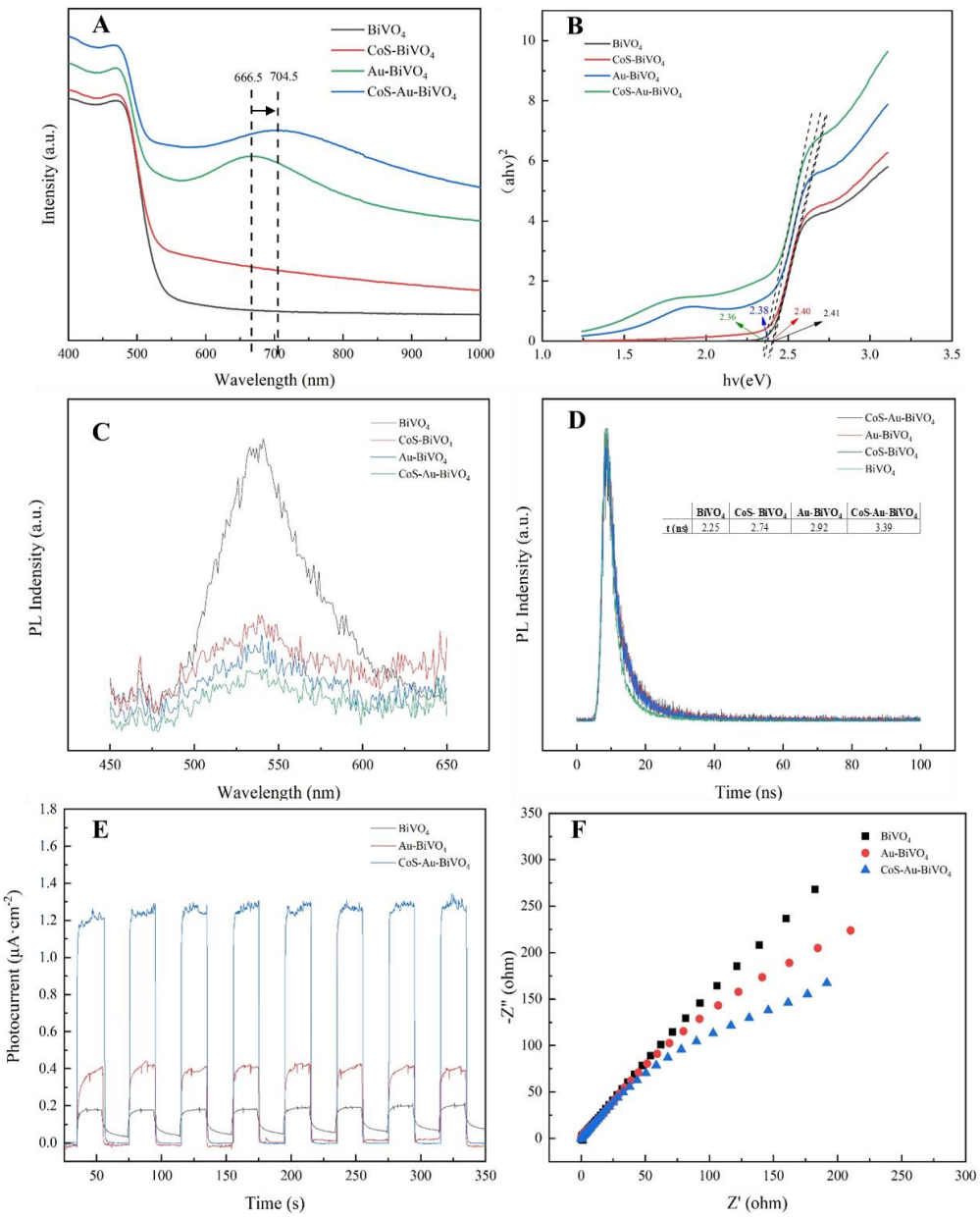

Figure 4. (**A**) UV-vis DRS spectra and (**B**) Tauc plots for $BiVO_4$, CoS-$BiVO_4$, Au-$BiVO_4$, and CoS-Au-$BiVO_4$. (**C**) PL spectra, (**D**) Time resolved spectroscopy, (**E**) Photocurrent and (**F**) EIS spectra for $BiVO_4$, CoS-$BiVO_4$, Au-$BiVO_4$, and CoS-Au-$BiVO_4$.

Mott–Schottky (MS) measurements were conducted to analyze the band structure, following the method in the Supplementary Materials and the result is shown in Figure 5. Since the conduction band (CB) of the n-type semiconductor is more negative (−0.2 eV) than the flat band, the CB of as-obtained $BiVO_4$ is 0.037 eV (vs. NHE). The Eg of $BiVO_4$ is 2.41 eV and the valence band (VB) is 2.37 as calculated. In the case of CoS-Au-$BiVO_4$, the composite also exhibited n-type and the more positive flat band of 0.08 eV (vs. Ag/AgCl). The loading of CoS led to a downward shift of the flat band, which facilitated the migration of photogenerated electrons and induced the formation of electrical field at the interfaces. Thus, this structure was able to accelerate the transfer of photogenerated electrons from $BiVO_4$ to Au NPs and, subsequently, to CoS.

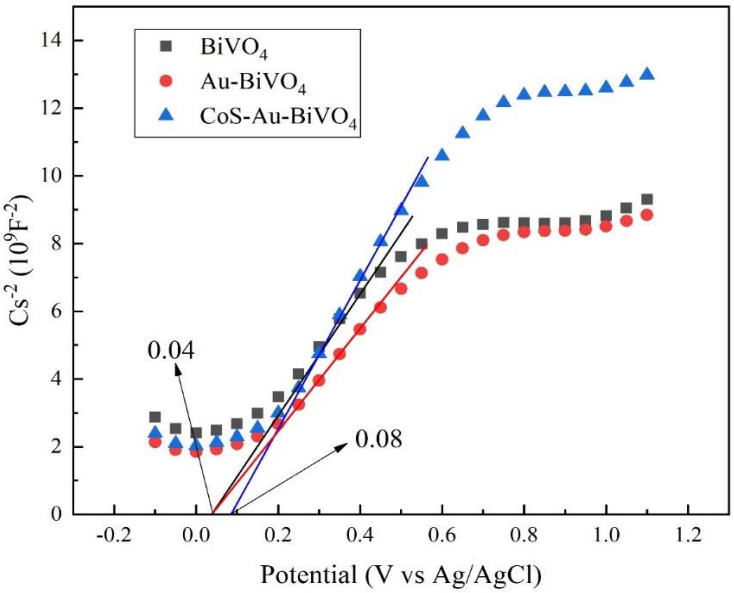

Figure 5. Mott-Schottky plots of $BiVO_4$, Au-$BiVO_4$, and CoS-Au-$BiVO_4$.

2.2. Photo-Assisted PMS Activation for Degradation of RhB

The experiment was conducted by the degradation of 10 ppm RhB with the addition of 0.1 M PMS and 0.5 g/L of the catalyst under the irradiation of visible light (wavelength > 420 nm). As shown in Figure 6A, RhB was hardly removed in the absence of PMS, which indicated that the photocatalytic reaction system cannot directly degrade RhB. However, as PMS was added to the reaction system, RhB removal followed the order of CoS-Au-$BiVO_4$/PMS/vis > Au-$BiVO_4$/PMS/vis > CoS-Au-$BiVO_4$/PMS/dark. Notably, CoS-Au-$BiVO_4$/PMS/vis achieved the highest degradation kinetics rate (k = 0.1381) which is much higher than Au-$BiVO_4$/PMS/vis (k = 0.0449) and CoS-Au-$BiVO_4$/PMS/dark (k = 0.0304) (Figure 6B). This excellent photocatalytic activity was probably due to the synergetic effects of the photogenerated carriers and PMS, which are discussed in detail in Section 3.5. To confirm the optimal content of the catalyst composition, different contents of Au and CoS were deposited on {010} facets of $BiVO_4$. The RhB removal increased as CoS content increased from 10% to 30%. However, excess loading of CoS inhibited light absorption and decreased photocatalytic activity (Figure S1). In addition, the optimal content of Au loaded on CoS-Au-$BiVO_4$ was 3% because large quantities of Au NPs were able to aggregate into large size particles with relatively low activity. Thus, CoS(30%)-Au(3%)-$BiVO_4$ exhibited the highest photocatalytic activity (Figure 6C). Moreover, 30%CoS-3%Au-$BiVO_4$ achieved the best reusability (Figure 6D). Even after five cycles, more than 90% of the RhB could be removed. The leaching of Co ions in each cycle was determined by AAS (Atomic Absorption Spectrometry). The concentrations of Co ions are 0.2 mg/L and 0.08 mg/L in reaction system at the first and second cycle, respectively (Table S2). But at the third cycle, Co ions were not detected in solution, which suggested high stability of CoS-Au-$BiVO_4$. Such low leaching of Co might be attributed to the combination of CoS and Au-$BiVO_4$. The

slight decrease in activity might be expressed by the loss of catalysts during the separation and recovery process of each cycle.

The influence of catalyst concentration on RhB degradation was conducted (Figure S2). Although an increase in the catalyst dosage could enhance the RhB degradation, the RhB degradation rate was slightly improved as the catalyst concentration increased from 0.5 g/L to 1 g/L. In considering a reduction in catalyst dosage, 0.5 g/L was selected as the optimal catalyst dosage. The influence of initial pH on RhB degradation was conducted (Figure S2). In addition, the highest catalytic activity was achieved at pH 7.22. RhB degradation was decreased both in the acidic condition and in the alkaline condition. On one hand, CoS might be dissolved in acidic condition, which decreased the catalytic stability of CoS-Au-$BiVO_4$. On the other hand, OH^- could be oxidized by $\bullet SO_4^-$ to generate •OH with lower oxidative ability and a shorter lifetime ($\bullet SO_4^- + OH^- \rightarrow SO_4^{2-} + \bullet OH$). Furthermore, pH changes before and after the reaction were also detected, which indicated that the pH value decreased from 7.22 to 5.13 after the reaction. This phenomenon can be explained as follows: (1) OH^- was consumed during the reaction ($h^+ + OH^- \rightarrow \bullet OH$, $\bullet SO_4^- + OH^- \rightarrow SO_4^{2-} + \bullet OH$, $\bullet OH + RhB \rightarrow$ products), resulting in a decrease of pH. (2) Some intermediates of RhB were low molecular weight acids, which also decreased the pH value.

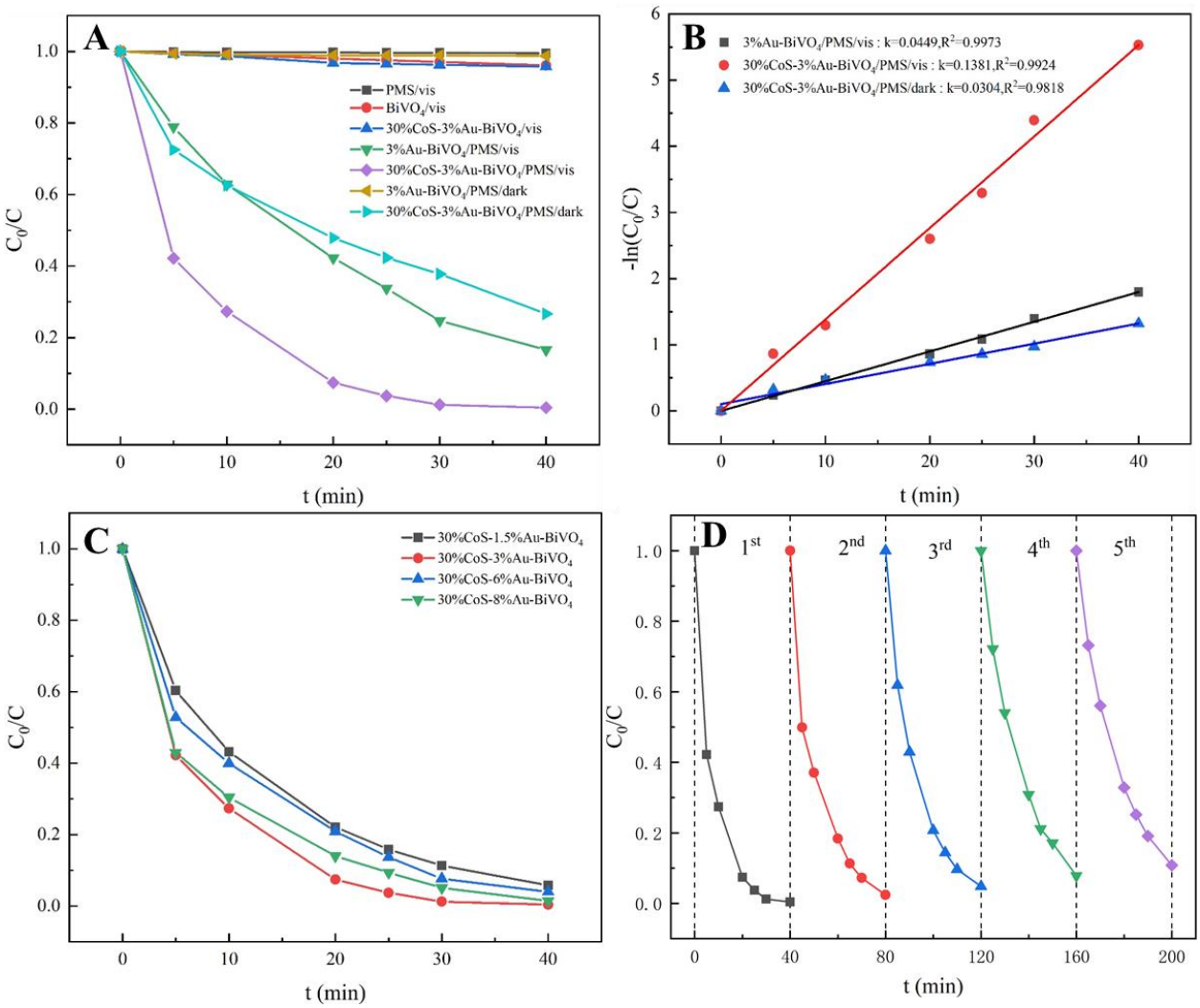

Figure 6. (**A**) Degradation of RhB over different samples and experiment parameters, (**B**) degradation kinetic curves of RhB, (**C**) degradation of RhB by PMS/Vis/30%CoS-ωt%Au-$BiVO_4$, (**D**) successive cycles degradation of RhB by PMS/Vis/30%CoS-3%Au-$BiVO_4$.

2.3. Photodegradation of Wastewater by a Pilot-Scale Instrument

More than 80% of TOC was removable under the optimal reaction conditions (3 mM PMS, pH = 5, C3) (Figure 7A). Notably, during the continuous reaction process, TOC removal could be maintained at above 60% (Figure 7D), which indicates that the photo-assisted Fenton-like system exhibits high potential in wastewater treatment. In addition, after 120 h of the reaction, the CoS-Au-$BiVO_4$ loaded on glass fibers was not washed away (Figure S3). The characteristic peak of Co^{2+} $2p_{3/2}$ (780.79 eV) was still stronger than that of Co^{3+} $2p_{3/2}$ (779.89 eV), demonstrating that most of Co elements in the composites were Co^{2+} (Figure 7E). Inorganic salt in the wastewater did not cause the deactivation of the catalyst.

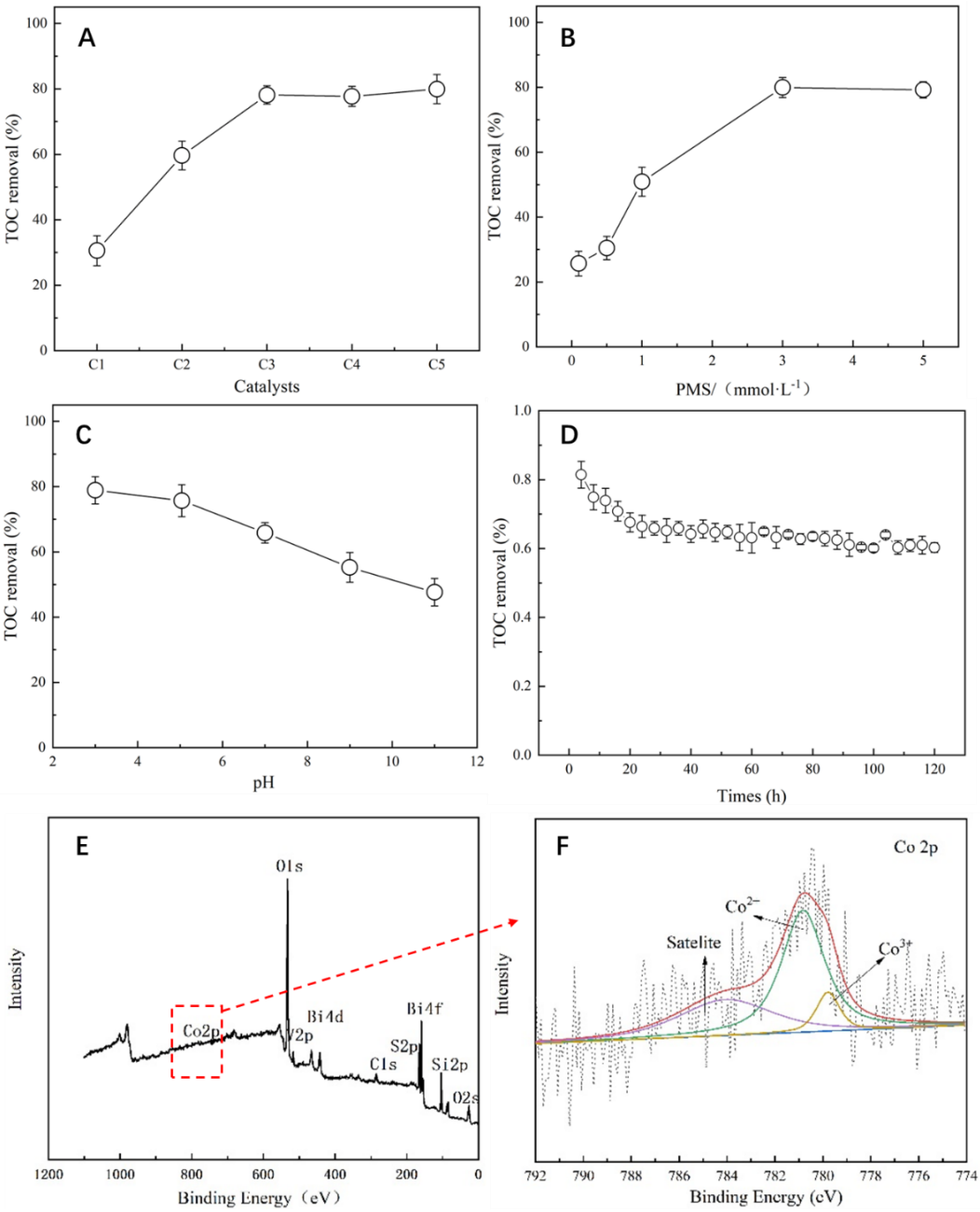

Figure 7. The influence of (**A**) loading amounts of catalysts (PMS = 3 mM, pH = 5.04), (**B**) PMS concentration (catalyst C3, pH = 5.04), (**C**) initial solution pH (catalyst C3, PMS = 3 mM) on the removal of TOC in wastewater; (**D**) Continuous batch operation test lasting for 120 h (catalyst C3, PMS = 3 mM, pH = 5.04); The XPS spectra of glass fiber and high resolution of Co2p3 after reaction (**E**,**F**).

2.4. Mechanism of Photo-Assisted PMS Activation Reaction System

Free radical quenching experiments and electron paramagnetic resonance spectroscopy (EPR) measurements were conducted to identify the radicals during the reaction process. EDTA-2Na and superoxide dismutase (SOD) were used as scavengers of photogenerated holes (h^+) and $\bullet O^{2-}$, respectively. Methanol (MeOH) can quench both $\bullet SO_4^-$ and •OH while tert-Butanol (TBA) can only scavenge •OH. RhB removal was obviously inhibited by EDTA-2Na and MeOH while TBA and SOD did not show obvious inhibition for RhB removal (Figure 8A), which indicates that h^+ and $\bullet SO_4^-$ played dominant roles in the RhB degradation process. Moreover, EPR characteristic signals of $\bullet SO_4^-$ and •OH were not detected without PMS under dark conditions (Figure 8B). However, after visible-light irradiation for 2 min, the characteristic peak of DMPOx which arose from the overoxidation of DMPO by h^+, appeared. Under dark/PMS conditions, DMPO-$\bullet SO_4^-$ and DMPO-•OH radicals, which arose from the PMS activation by Co^{2+} and H_2O oxidation by $\bullet SO_4^-$, could be detected. Notably, both $\bullet SO_4^-$ and ·OH intensity were significantly increased under PMS/visible-light condition. Such an improvement can be explained as follows: (1) the heterojunctions promoted the transfer of photogenerated electrons to cobalt sulfide; (2) photogenerated electrons accelerated the redox of Co^{2+}/Co^{3+}, which enhanced the PMS activation by Co^{2+} for $\bullet SO_4^-$ generation; (3) the h^+ transferred from the bulk to the surface of {110}$BiVO_4$ for the degradation of organics.

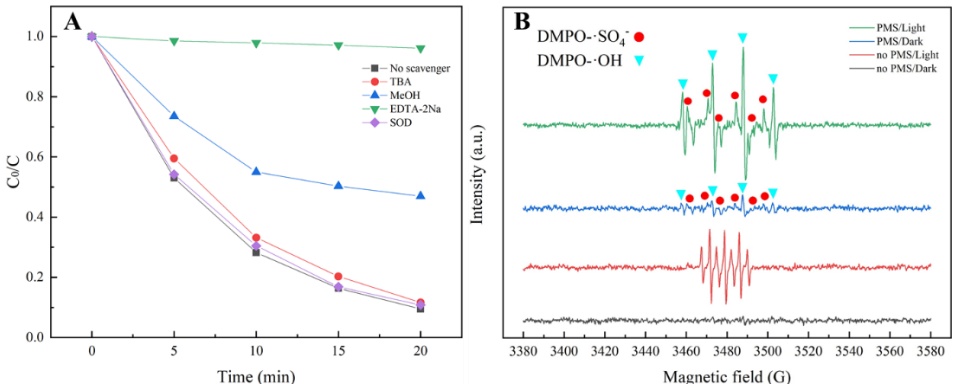

Figure 8. (**A**) Effect of radical scavengers on the degradation of RhB; (**B**) EPR spectra under various conditions.

Based on the above results, the possible photocatalytic mechanism is proposed as follows (Figure 9): (1) the photogenerated electrons are accumulated on the {010} facets of $BiVO_4$ due to the pre-separation effect (Equation (1)); (2) then, Schottky junctions constructed between Au NPs and $BiVO_4$ {010} facets facilitated the transfer of photogenerated electrons from $BiVO_4$ {010} facets to Au NPs; (3) PMS is reduced to $\bullet SO_4^-$ by Co^{2+}(Equation (2)), and CoS captures the photoelectrons from the Au NPs for acceleration of Co^{2+}/Co^{3+} redox (Equation (4)) because of its lower conduction band and higher work function, compared to Au. In addition, large quantities of photogenerated holes, which are attributed to the pre-separation effect and Schottky junctions, accumulated on the $BiVO_4$ {110} facets, which are also able to also degrade RhB (Equation (5)).Being attributed to unique structure of CoS-Au-$BiVO_4$, the reaction system efficiently inhibits the recombination of photocarriers (Equation (1)). CoS, in the composite of CoS-Au-$BiVO_4$, was able to activate PMS for the generation of $\bullet SO_4^-$ with the oxidation of Co^{2+} to Co^{3+} (Equation (2)). Meanwhile, photogenerated electrons from $BiVO_4$ were transferred to CoS via the medium of Au, which reduced Co^{3+} to Co^{2+} and enhanced the stability of the catalyst (Equation (4)). The oxidation of OH^- by $\bullet SO_4^-$ can produce •OH (Equation (3)). Both free radicals ($\bullet SO_4^-$, •OH) and h^+ are responsible for RhB degradation. Thus, the reaction system exhibits high activity and stability.

$$\text{CoS-Au-BiVO}_4 + \text{hv} \rightarrow e^- + h^+ \quad (1)$$

$$Co^{2+} + HSO_5^- \rightarrow Co^{3+} + \bullet SO_4^- + OH^- \quad (2)$$

$$\bullet SO_4^- + OH^- \rightarrow SO_4^{2-} + \bullet OH \quad (3)$$

$$Co^{3+} + e^- \rightarrow Co^{2+} \quad (4)$$

$$\bullet SO_4^- + h^+ + \bullet OH + \text{pollutants} \rightarrow \text{products} \quad (5)$$

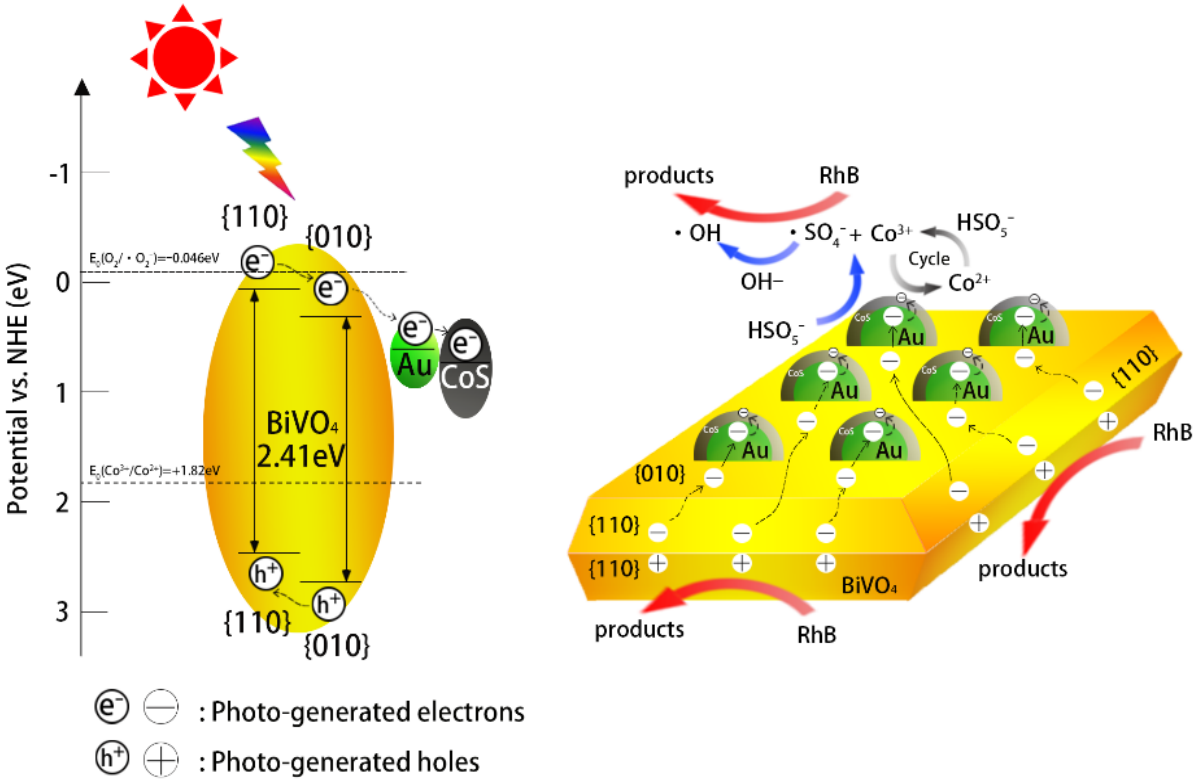

Figure 9. Possible photocatalytic mechanism of the PMS/Vis/CoS-Au-{010}$BiVO_4$ system.

3. Materials and Methods

3.1. Chemicals

$HAuCl_4 \cdot 3H_2O$ (>99.9%), S (>99.5%), $Bi(NO_3)_3 \cdot 5H_2O$ (>99%) and RhB were purchased from Aladdin Chemistry Co., Ltd., China. $Co(NO_3)_2 \cdot 6H_2O$ (>99%) and NH_4VO_3 (>99%) were purchased from Rhawn Reagent, Shanghai, China. $2KHSO_5 \cdot KHSO_4 \cdot 2K_2SO_4$ (PMS) and superoxide dismutase (SOD, u/mg) were purchased from Shanghai Macklin Biochemical Co., Ltd., China. Ethyl alcohol (Et-OH, >99%), methyl alcohol (Me-OH, >99.5%), tert butyl alcohol (TBA, >98%), NH_3H_2O (25–28%), $(NH_4)_2C_2O_4 \cdot H_2O$ (>99.8%) and EDTA-2Na (>99%) were purchased from Sino-pharm Chemical Reagent Co., Ltd. DMPO was purchased from Dojindo Laboratories, Shanghai, China. All chemicals were analytical reagents without further purification.

3.2. Synthesis of Photoassisted Fenton-like Catalyst

Synthesis of m-$BiVO_4$: m-$BiVO_4$ was synthesized by a hydrothermal process according to the previous studies [27]. Typically, 485 mg $Bi(NO_3)_3 \cdot 5H_2O$ and 117 mg NH_4VO_3 were respectively dissolved in 30 mL of 2 M HNO_3. After ultra-sonicated for 10 min, $Bi(NO_3)_3$ solution was added into NH_4VO_3 drop by drop under magnetic stirring. Then, the pH was adjusted to 1.5 using NH_3 H_2O and the mixture was stirred for 2 h, followed by heating at 200 °C for 12 h in a 100 mL Teflon-lined stainless-steel autoclave. The yellow powder, which was finally obtained, was separated and washed with distilled water several times, and dried at 60 °C.

Selective photo-deposition of Au on the {010} facet of m-$BiVO_4$: Photogenerated electrons were accumulated on the {010} facet of m-$BiVO_4$ for the different energy band structure of {010} and {110} facets. Thus, Au nanoparticles could be selectively photo-deposited on the {010} facets while $HAuCl_4 \cdot 3H_2O$ acted as precursor and $(NH_4)_2C_2O_4 \cdot H_2O$ acted as hole scavenger. Typically, 0.1 g m-$BiVO_4$ and a certain amount of $HAuCl_4 \cdot 3H_2O$ (1 mM) (Au of $HAuCl_4 \cdot 3H_2O$: $BiVO_4$ = 1.5 wt%, 3 wt%, 6 wt%, 8 wt%) were mixed in ultrapure water with magnetic stirring for 30 min. Then, $(NH_4)_2C_2O_4 \cdot H_2O$ was added to the mixture; this was followed by irradiation from a 350 W Xe lamp. After reaction for 2 h, the residue (Au-$BiVO_4$) was washed and dried.

Synthesis of CoS-Au-$BiVO_4$: S adsorbed on Au nanoparticles could be reduced to S^{2-} by photoelectrons of m-$BiVO_4$ [29,35]. Typically, 50 mg Au-$BiVO_4$ and certain amounts of S powder were dispersed in 50 mL ethanol with magnetic stirring, under the protection of N_2 in the dark for 1.5 h. Then, a certain amount of $Co(NO_3)_2 \cdot 6H_2O$ (molar ratio of S: $Co(NO_3)_2 \cdot 6H_2O$ = 1:1) was added to the mixture with magnetic stirring under the irradiation of a 350 W Xe lamp for 2 h. The residue (CoS-Au-$BiVO_4$) collected by centrifugation was washed with deionized water and dried at 70 °C.

CoS-Au-$BiVO_4$ loaded on glass fiber: Before the loading of CoS-Au-$BiVO_4$, glass fibers with the thickness of 0.1 mm were immersed in 0.1 M HNO_3 for 2 h and then washed with deionized water. After calcination in a muffle furnace at 400 °C for 2 h, the glass fibers were cut into squares with lengths of 10 cm each. Then, CoS-Au-$BiVO_4$ was mixed with silica sol (CoS-Au-$BiVO_4$: silica sol = 5:2), and the mixture was surface-coated on glass fibers using a spray gun. The glass fiber coated with CoS-Au-$BiVO_4$ was dried at 70 °C. In the present work, glass fibers coated with different amounts of CoS-Au-$BiVO_4$ (0.2 g, 0.5 g, 0.7 g, 1 g, 1.5 g) were prepared.

3.3. Catalyst Characterization

The morphologies of the prepared catalysts and the distribution of elements on their surface were observed by utilizing scanning electron microscopy (SEM) (FEI Co., Ltd., FEG250, Hillsboro, OR, USA) with Energy Dispersive X-ray Spectroscopy (EDX). To further determine the Au@CoS core-shell microstructure on the $BiVO_4$ {010} facets, transmission electron microscopy (TEM) (JEOL Co., Ltd., JEM2800, Tokyo, Japan) with EDX was also utilized. X-ray diffractometry (XRD) (Bruker Co., Ltd., D8 Advance, Karlsruhe, Germany) patterns were obtained to analyze the crystalline structure of the composites. The el ement states of the samples were recorded by PHI5000 X-ray photoelectron spectroscopy (XPS). The UV-vis diffuse reflectance spectra of the catalysts were analyzed to evaluate the light response (λ = 400–1000 nm) using a Shimadzu UV2600 spectrophotometer. Electrochemical impedance spectra (EIS), Mott–Schottky (MS) and photocurrent measurements were conducted on the CHI660E workstation in 0.5 M Na_2SO_4 solution with a three-electrode system consisting of a Pt auxiliary electrode, AgCl reference electrode and study electrode slice. The photoluminescence (PL) spectra of the synthesized samples were detected on a Hitachi F7000 spectrophotometer.

3.4. Photocatalytic Activity and Stability Tests

The photocatalytic activity of the samples was tested by photo-degradation of Rhodamine B (RhB) under the irradiation of a 350 W Xe lamp with a 420 nm filter, in both the presence and the absence of PMS, and the light intensity of the Xe lamp was 96 mW/cm^2. To obtain the optimal contents of Au and CoS in the CoS-Au-$BiVO_4$ composite, the photocatalytic activity of various samples (Au of $HAuCl_4 \cdot 3H_2O$: $BiVO_4$ = 1.5–8 wt%, CoS: Au-$BiVO_4$ = 3–40 wt%) was tested as follows: 25 mg of catalyst was added in 50 mL of 10 mg/L RhB solution with stirring for 30 min in the dark to achieve the adsorption-desorption equilibrium between catalysts and RhB. Then, 100 μL PMS (0.05 M) was added to the mixture, and then kept the mixture under the irradiation for 40 min. During the reaction process, 3 mL of the samples was periodically withdrawn, and methanol was used to quench the radicals. The absorbance of RhB was measured in order to analyze the

residual concentration of RhB, using the Shimadzu UV2600 at 554 nm, and the degradation efficiency (η) and kinetic constants were calculated. The concentrations of Co ion in solution were measured by Atomic Absorption Spectrometry (AAS) (Thermo Scientific Co., Ltd., ICE3500, Waltham, MA, USA).

3.5. Mechanism of Photo-Assisted Fenton-like System

The experiments for quenching free radicals were carried out to illustrate the catalytic mechanism using different scavengers: Ethylenediamine tetra acetic acid disodium salt (EDTA-2Na) for quenching h^+, Superoxide dismutase (SOD) for quenching $\cdot O_2^-$, methanol (Me-OH) for quenching $\cdot SO_4^-$, tert-Butanol (TBA) for quenching (·OH). The degradation process was similar to the experiment of catalytic activity, except that 10 mM of certain scavengers was added into the mixture in advance. Then, the EPR signals of the active radicals were scavenged by DMPO on a Bruker EMX-10/12 spectrometer.

3.6. Photoatalytic Degradation of Wastewater by a Pilot-Scale Instrument

A pilot scale experiment was conducted to evaluate the catalytic performance for practical wastewater degradation. The wastewater quality is listed in Table S3. The weight of photocatalysts in synthesized samples are listed in Table S4. The reactor volume was 50 L, and the glass fiber coated with CoS-Au-$BiVO_4$ was surrounded an Xe lamp (2000 W). The sequencing batch reaction time was 4 h in order to ensure sufficient TOC degradation. In order to optimize the operation conditions, the influence of pH, catalyst and PMS dose on TOC removal was tested. Then, the pilot scale reaction system ran continuously for 120 h, which might provide more useful information for practical application.

4. Conclusions

Novel visible-light response photocatalyst CoS-Au-$BiVO_4$ was fabricated to construct a photo-assisted PMS activation system, which could retard the accumulation of high-valence-state transition metal during the Fenton-like reaction process. $BiVO_4$ could act as the 'pre-separation channel', which promoted the transfer of photogenerated electrons from the m-$BiVO_4$ {010} facet to Au. The photogenerated electrons were subsequently captured by CoS for PMS activation. On the other hand, holes, accumulated on the m-$BiVO_4$ {110} facets, were also able to oxidize organics. Thus, the main species for the degradation of organics were the sulfate radical ($\bullet SO_4^-$) and the photogenerated hole (h^+). More than 95% RhB could be degraded within 40 min. Even after five cycles, 80% of RhB was still removed. Moreover, the pilot scale experiment indicated that CoS-Au-$BiVO_4$ loaded on glass fiber is effectively able to mineralize organic pollutants in practical wastewater, suggesting a high potential for application in engineering. This work also provides a simple method for constructing a photo-Fenton-like reaction system, which can utilize photogenerated carriers for transition metal redox and PMS activation.

Supplementary Materials: The following are available online at https://www.mdpi.com/article/10.3390/catal11111414/s1, the specific methods for Mott–Schottky measurement; Figure S1: Photodegradation of RhB by different synthesized samples of (A) wt%CoS-1.5%Au-$BiVO_4$, (B) wt%CoS-3%Au-$BiVO_4$, (C)wt%CoS-6%Au-$BiVO_4$ and (D) wt%CoS-8%Au-$BiVO_4$; Figure S2: Effects of catalyst dosage (A) and pH (B) for degradation of RhB by CoS-Au-BiVO4/PMS/Vis; Figure S3: The pictures of pure and prepared glass fiber (A,B); the picture and SEM image of glass fiber after reaction (C,D); Table S1. The atomic concentrations of elements in CoS-Au-$BiVO_4$; Table S2. The Co ion concentrations in solutions after cycling experiments; Table S3: Water quality parameters of wastewater; Table S4: The weight of photocatalysts in samples of C1~C5.

Author Contributions: Conceptualization, J.W.; methodology, Y.J.; data curation, Y.J., Y.Z. and W.B.; formal analysis, Y.Z.; investigation, Y.J. and Y.Z.; project administration, J.W.; supervision, J.W.; validation, A.L. and P.F.-X.C.; writing—original draft preparation, Y.J.; writing—review and editing, J.W. All authors have read and agreed to the published version of the manuscript.

Funding: This research was supported by the National Natural Science Foundation of China (No. 51878335 and No. 52070095) and the Natural Science Foundation of Jiangsu province (BK20191255).

Data Availability Statement: The data presented in this study are openly available.

Conflicts of Interest: The authors declare no conflict of interest.

References

1. Zhu, C.; Liu, F.; Ling, C.; Jiang, H.; Wu, H.; Li, A. Growth of graphene-supported hollow cobalt sulfide nanocrystals via MOF-templated ligand exchange as surface-bound radical sinks for highly efficient bisphenol A degradation. *Appl. Catal. B Environ.* **2019**, *242*, 238–248. [CrossRef]
2. Gong, Y.; Zhao, X.; Zhang, H.; Yang, B.; Xiao, K.; Guo, T.; Zhang, J.; Shao, H.; Wang, Y.; Yu, G. MOF-derived nitrogen doped carbon modified g-C_3N_4 heterostructure composite with enhanced photocatalytic activity for bisphenol A degradation with peroxymonosulfate under visible light irradiation. *Appl. Catal. B Environ.* **2018**, *233*, 35–45. [CrossRef]
3. Wang, J.; Wang, S. Activation of persulfate (PS) and peroxymonosulfate (PMS) and application for the degradation of emerging contaminants. *Chem. Eng. J.* **2018**, *334*, 1502–1517. [CrossRef]
4. Oh, W.-D.; Dong, Z.; Lim, T.-T. Generation of sulfate radical through heterogeneous catalysis for organic contaminants removal: Current development, challenges and prospects. *Appl. Catal. B Environ.* **2016**, *194*, 169–201. [CrossRef]
5. Hu, P.; Long, M. Cobalt-catalyzed sulfate radical-based advanced oxidation: A review on heterogeneous catalysts and applications. *Appl. Catal. B Environ.* **2016**, *181*, 103–117. [CrossRef]
6. Giannakis, S.; Lin, K.-Y.A.; Ghanbari, F. A review of the recent advances on the treatment of industrial wastewaters by Sulfate Radical-based Advanced Oxidation Processes (SR-AOPs). *Chem. Eng. J.* **2021**, *406*, 127083. [CrossRef]
7. Zhou, X.; Luo, M.; Xie, C.; Wang, H.; Wang, J.; Chen, Z.; Xiao, J.; Chen, Z. Tunable S doping from Co_3O_4 to Co_9S_8 for peroxymonosulfate activation: Distinguished Radical/Nonradical species and generation pathways. *Appl. Catal. B Environ.* **2021**, *282*, 119605. [CrossRef]
8. Chen, L.; Ji, H.; Qi, J.; Huang, T.; Wang, C.-C.; Liu, W. Degradation of acetaminophen by activated peroxymonosulfate using $Co(OH)_2$ hollow microsphere supported titanate nanotubes: Insights into sulfate radical production pathway through CoOH+ activation. *Chem. Eng. J.* **2021**, *406*, 126877. [CrossRef]
9. Lin, K.A.; Chen, B.J. Prussian blue analogue derived magnetic carbon/cobalt/iron nanocomposite as an efficient and recyclable catalyst for activation of peroxymonosulfate. *Chemosphere* **2017**, *166*, 146–156. [CrossRef] [PubMed]
10. Shao, H.; Zhao, X.; Wang, Y.; Mao, R.; Wang, Y.; Qiao, M.; Zhao, S.; Zhu, Y. Synergetic activation of peroxymonosulfate by Co_3O_4 modified g-C_3N_4 for enhanced degradation of diclofenac sodium under visible light irradiation. *Appl. Catal. B Environ.* **2017**, *218*, 810–818. [CrossRef]
11. Wang, H.; Wang, C.; Cui, X.; Qin, L.; Ding, R.; Wang, L.; Liu, Z.; Zheng, Z.; Lv, B. Design and facile one-step synthesis of $FeWO_4/Fe_2O_3$ di-modified WO3 with super high photocatalytic activity toward degradation of quasi-phenothiazine dyes. *Appl. Catal. B Environ.* **2018**, *221*, 169–178. [CrossRef]
12. Wang, Y.; Liu, C.; Zhang, Y.; Meng, W.; Yu, B.; Pu, S.; Yuan, D.; Qi, F.; Xu, B.; Chu, W. Sulfate radical-based photo-Fenton reaction derived by $CuBi_2O_4$ and its composites with α-Bi_2O_3 under visible light irradiation: Catalyst fabrication, performance and reaction mechanism. *Appl. Catal. B Environ.* **2018**, *235*, 264–273. [CrossRef]
13. Gao, H.; Yang, H.; Xu, J.; Zhang, S.; Li, J. Strongly Coupled g-C_3N_4 Nanosheets-Co_3O_4 Quantum Dots as 2D/0D Heterostructure Composite for Peroxymonosulfate Activation. *Small* **2018**, *14*, e1801353. [CrossRef]
14. Tan, H.L.; Wen, X.; Amal, R.; Ng, Y.H. $BiVO_4$ {010} and {110} Relative Exposure Extent: Governing Factor of Surface Charge Population and Photocatalytic Activity. *J. Phys. Chem. Lett.* **2016**, *7*, 1400–1405. [CrossRef]
15. Li, R.; Zhang, F.; Wang, D.; Yang, J.; Li, M.; Zhu, J.; Zhou, X.; Han, H.; Li, C. Spatial separation of photogenerated electrons and holes among {010} and {110} crystal facets of $BiVO_4$. *Nat. Commun.* **2013**, *4*, 1432. [CrossRef]
16. Liu, L.; Jiang, Y.; Zhao, H.; Chen, J.; Cheng, J.; Yang, K.; Li, Y. Engineering Coexposed {001} and {101} Facets in Oxygen-Deficient TiO_2 Nanocrystals for Enhanced CO_2 Photoreduction under Visible Light. *ACS Catal.* **2016**, *6*, 1097–1108. [CrossRef]
17. Zhao, Y.; Li, R.; Mu, L.; Li, C. Significance of Crystal Morphology Controlling in Semiconductor-Based Photocatalysis: A Case Study on $BiVO_4$ Photocatalyst. *Cryst. Growth Des.* **2017**, *17*, 2923–2928. [CrossRef]
18. Li, R.; Han, H.; Zhang, F.; Wang, D.; Li, C. Highly efficient photocatalysts constructed by rational assembly of dual-cocatalysts separately on different facets of $BiVO_4$. *Energy Environ. Sci.* **2014**, *7*, 1369–1376. [CrossRef]
19. Li, C.; Zhang, P.; Lv, R.; Lu, J.; Wang, T.; Wang, S.; Wang, H.; Gong, J. Selective deposition of Ag_3PO_4 on monoclinic $BiVO_4$(040) for highly efficient photocatalysis. *Small* **2013**, *9*, 3951–3956. [CrossRef]
20. Zhou, C.; Wang, S.; Zhao, Z.; Shi, Z.; Yan, S.; Zou, Z. A Facet-Dependent Schottky-Junction Electron Shuttle in a $BiVO_4$.{010}-Au-Cu_2O Z-Scheme Photocatalyst for Efficient Charge Separation. *Adv. Funct. Mater.* **2018**, *28*, 1801214. [CrossRef]
21. Abdi, F.F.; Firet, N.; van de Krol, R. Efficient $BiVO_4$Thin Film Photoanodes Modified with Cobalt Phosphate Catalyst and W-doping. *ChemCatChem* **2013**, *5*, 490–496. [CrossRef]
22. Hirakawa, H.; Shiota, S.; Shiraishi, Y.; Sakamoto, H.; Ichikawa, S.; Hirai, T. Au Nanoparticles Supported on $BiVO_4$: Effective Inorganic Photocatalysts for H_2O_2 Production from Water and O_2 under Visible Light. *ACS Catal.* **2016**, *6*, 4976–4982. [CrossRef]

23. Wang, H.; Zhang, L.; Chen, Z.; Hu, J.; Li, S.; Wang, Z.; Liu, J.; Wang, X. Semiconductor heterojunction photocatalysts: Design, construction, and photocatalytic performances. *Chem. Soc. Rev.* **2014**, *43*, 5234–5244. [CrossRef] [PubMed]
24. Liu, X.; Iocozzia, J.; Wang, Y.; Cui, X.; Chen, Y.; Zhao, S.; Li, Z.; Lin, Z. Noble metal–metal oxide nanohybrids with tailored nanostructures for efficient solar energy conversion, photocatalysis and environmental remediation. *Energy Environ. Sci.* **2017**, *10*, 402–434. [CrossRef]
25. Hou, Z.; Chen, F.; Wang, J.; François-Xavier, C.P.; Wintgens, T. Novel Pd/$GdCrO_3$ composite for photo-catalytic reduction of nitrate to N_2 with high selectivity and activity. *Appl. Catal. B Environ.* **2018**, *232*, 124–134. [CrossRef]
26. Low, J.; Yu, J.; Jaroniec, M.; Wageh, S.; Al-Ghamdi, A.A. Heterojunction Photocatalysts. *Adv. Mater.* **2017**, *29*, 1601694. [CrossRef]
27. Chen, F.; Wu, C.; Wang, J.; François-Xavier, C.P.; Wintgens, T. Highly efficient Z-scheme structured visible-light photocatalyst constructed by selective doping of Ag@AgBr and Co_3O_4 separately on {010} and {110} facets of $BiVO_4$: Pre-separation channel and hole-sink effects. *Appl. Catal. B Environ.* **2019**, *250*, 31–41. [CrossRef]
28. Zhu, H.; Ji, Y.; Chen, L.; Bian, W.; Wang, J. Pt Nanowire-Anchored Dodecahedral Ag_3PO_4{110} Constructed for Significant Enhancement of Photocatalytic Activity and Anti-Photocorrosion Properties: Spatial Separation of Charge Carriers and PhotogeneratedElectron Utilization. *Catalysts* **2020**, *10*, 206. [CrossRef]
29. Tada, H.; Mitsui, T.; Kiyonaga, T.; Akita, T.; Tanaka, K. All-solid-state Z-scheme in CdS-Au-TiO_2 three-component nanojunction system. *Nat. Mater.* **2006**, *5*, 782–786. [CrossRef]
30. Ding, Y.B.; Tang, H.B.; Zhang, S.H.; Wang, S.B.; Tang, H.Q. Efficient degradation of carbamazepine by easily recyclable microscaled $CuFeO_2$ mediated heterogeneous activation of peroxymonosulfate. *J. Hazard. Mater.* **2016**, *317*, 686–694. [CrossRef]
31. Golshan, M.; Kakavandi, B.; Ahmadi, M.; Azizi, M. Photocatalytic activation of peroxymonosulfate by TiO_2 anchored on cupper ferrite (TiO_2@$CuFe_2O_4$) into 2,4-D degradation: Process feasibility, mechanism and pathway. *J. Hazard. Mater.* **2018**, *359*, 325–337. [CrossRef] [PubMed]
32. Zhang, J.; Zhao, X.; Wang, Y.; Gong, Y.; Cao, D.; Qiao, M. Peroxymonosulfate-enhanced visible light photocatalytic degradation of bisphenol A by perylene imide-modified g-C_3N_4. *Appl. Catal. B Environ.* **2018**, *237*, 976–985. [CrossRef]
33. Chen, Q.; Ji, F.; Liu, T.; Yan, P.; Guan, W.; Xu, X. Synergistic effect of bifunctional Co–TiO_2 catalyst on degradation of Rhodamine B: Fenton-photo hybrid process. *Chem. Eng. J.* **2013**, *229*, 57–65. [CrossRef]
34. Bao, S.; Wu, Q.; Chang, S.; Tian, B.; Zhang, J. Z-scheme CdS–Au–$BiVO_4$ with enhanced photocatalytic activity for organic contaminant decomposition. *Catal. Sci. Technol.* **2017**, *7*, 124–132. [CrossRef]
35. Ye, F.; Li, H.; Yu, H.; Chen, S.; Quan, X. Constructing $BiVO_4$-Au@CdS photocatalyst with energic charge-carrier-separation capacity derived from facet induction and Z-scheme bridge for degradation of organic pollutants. *Appl. Catal. B Environ.* **2018**, *227*, 258–265. [CrossRef]
36. Ingram, D.B.; Christopher, P.; Bauer, J.L.; Linic, S. Predictive Model for the Design of Plasmonic Metal/Semiconductor Composite Photocatalysts. *ACS Catal.* **2011**, *1*, 1441–1447. [CrossRef]
37. Shaik, F.; Peer, I.; Jain, P.K.; Amirav, L. Plasmon-Enhanced Multicarrier Photocatalysis. *Nano Lett.* **2018**, *18*, 4370–4376. [CrossRef]
38. Hou, W.; Cronin, S.B. A Review of Surface Plasmon Resonance-Enhanced Photocatalysis. *Adv. Funct. Mater.* **2013**, *23*, 1612–1619. [CrossRef]
39. Mane, S.T.; Kamble, S.S.; Deshmukh, L.P. Cobalt sulphide thin films: Chemical bath deposition, growth and properties. *Mater. Lett.* **2011**, *65*, 2639–2641. [CrossRef]
40. Cai, P.; Huang, J.; Chen, J.; Wen, Z. Oxygen-Containing Amorphous Cobalt Sulfide Porous Nanocubes as High-Activity Electrocatalysts for the Oxygen Evolution Reaction in an Alkaline/Neutral Medium. *Angew. Chem. Int. Ed.* **2017**, *56*, 4858–4861. [CrossRef]
41. Tada, H.; Suzuki, F.; Ito, S.; Akita, T.; Tanaka, K.; Kawahara, T.; Kobayashi, H. Au-Core/Pt-Shell Bimetallic Cluster-Loaded TiO_2. 1. Adsorption of Organosulfur Compound. *J. Phys. Chem. B* **2002**, *106*, 8714–8720. [CrossRef]
42. She, H.; Jiang, M.; Yue, P.; Huang, J.; Wang, L.; Li, J.; Zhu, G.; Wang, Q. Metal (Ni^{2+}/Co^{2+}) sulfides modified $BiVO_4$ for effective improvement in photoelectrochemical water splitting. *J. Colloid Interface Sci.* **2019**, *549*, 80–88. [CrossRef] [PubMed]